Electrochemical Study of a Pendant Molten Alumina Droplet and Its Application for Thermodynamic Property Measurements of Al-Ir

Electrochemical Study of a Pendant Molten Alumina Droplet and Its Application for Thermodynamic Property Measurements of Al-Ir

Bradley R. Nakanishi and Antoine Allanore[*,z]

Department of Materials Science and Engineering, Massachusetts Institute of Technology, Cambridge, Massachusetts 02139, USA

Limited knowledge of the thermodynamic and transport properties of refractory materials in the liquid state remains a key challenge limiting their application. Using alternating current (AC) and direct current (DC) techniques, the electrochemical kinetics of oxygen evolution and metal deposition was investigated in a pendant droplet of molten alumina (Al_2O_3) with three iridium (Ir) electrodes in a thermal imaging furnace. For the first time, the direct electrolytic decomposition of molten Al_2O_3 to oxygen gas and aluminum (Al) metal (alloyed with Ir) was observed, confirming the ionic nature of molten Al_2O_3. The decomposition potential of molten Al_2O_3 was measured with high precision using AC voltammetry, and the results demonstrated remarkable sensitivity to variation in temperature enabling measurement of chemical potential and entropy of Al at the Ir-rich solid-liquid phase boundary for the first time. The results were in remarkably close agreement with the most recent thermodynamic assessment of the Al-Ir system.

Manuscript submitted June 28, 2017; revised manuscript received October 5, 2017. Published October 25, 2017.

Structural materials developed for lasers, nuclear, aerospace or materials processing are required to sustain high temperature, and therefore often rely on solid refractory materials, e.g. iridium-based superalloys exhibiting exceptional corrosion and creep resistance.[1] The ultimate temperature of stability for those solid phases is captured in the phase diagram by their equilibrium with the liquid phase, usually found at ultra-high temperature (UHT, $T > 2000$ K). For the refractory oxides, where herein the adjective "refractory" relates to a metal oxide more stable than SiO_2 (e.g. Al_2O_3), the chemical bonding responsible for their stability in the solid-state also contributes to their UHT melting points. Unfortunately, information for materials at UHT in both condensed states remains extremely limited.[2–5] In particular, property prediction for melts by ab initio techniques remains time consuming and limited to specific compositions and temperatures, and their validation requires reliable experimental data.[6]

Limited information for refractory melts is derived from the difficulty of UHT experiments. For example, containment selection remains a critical step and a key challenge. Interestingly, the difficulty for containment selection also stems from a lack of thermodynamic and reaction kinetic information for refractory materials. Reviews of existing techniques for thermodynamic property measurement of refractory melts are found elsewhere.[5,7] The state of the art relies primarily on equilibration,[5] calorimetry,[8,9] and diffraction measurements.[10,11] These methods can provide phase-transition temperatures, enthalpies of formation or heat capacities, but only vapor pressure or electromotive force (emf) measurements provide direct access to chemical potentials (Gibbs energy), the quintessential thermodynamic quantity for phase diagram boundaries prediction.[7] Unfortunately, vapor pressure measurements are rarely feasible for refractory melts, exhibiting particularly low vapor pressures typically, and emf methods ordinarily require an ion-selective membrane,[12] an additional materials challenge at UHT.

However, given the nature of their bonding, refractory oxide melts can be postulated to exhibit ionic behavior upon fusion, enabling property measurements at UHT by electrochemical methods. Using these materials as electrolytes could enable determination of chemical potential and entropy, along with transport properties, such as diffusivity or electrical conductivity as demonstrated extensively in silicate melts.[3,13–18] To date, however, no electrochemical techniques have been demonstrated in molten oxides above 2000 K.

Given the likelihood of contamination of the refractory melts at UHT, containerless approaches are preferred, such as electrostatic,[19] aerodynamic[20–22] or acoustic[23,24] levitation techniques. While these methods are currently preferred for measuring structure,[10,11,25,26] total conductivity,[21] density, viscosity and surface tension[24,27] or even integral thermodynamic properties,[28] the sample size is necessarily small (1–4 mm) and each method is limited to their respective subset of compatible atmospheres (e.g. vacuum only for electrostatic levitation). Furthermore, all of these methods preclude electrochemical investigation as contacting electrodes to a droplet interfere with its levitation. As a matter of fact, no studies utilizing levitation have reported partial thermodynamic properties to date.

An alternative containerless approach handling a larger amount of material is the pendant droplet technique. This technique originated with the rise of the thermal imaging (or arc imaging) furnace (TIF),[29] which was extensively developed for and is nearly exclusively associated with the floating zone crystal growth method.[30–33] Historically, TIFs provided for the first time "essentially unlimited" temperature ranges for melting essentially any material in "practically any atmosphere".[32] Despite their focus on improving crystal growth at the time, Field and Wagner[32] suggested that "the technique can be utilized for other high temperature experiments of importance to material research . . . ". Diamond and Dragoo were among the first to take advantage of these opportunities to directly observe the solubility of gases (Ar, O_2, H_2, H_2O, N_2, and He) and their effects on vaporization behavior of molten pendant droplets of Al_2O_3.[34] Soon after the advent of lasers, they were utilized as a heat source in TIFs for their superior heating efficiency.[35,36] For example, Nelson et al. revisited the solubility of gaseous species in molten Al_2O_3 and their effects on solidification.[37] Later, Krishnan et al. measured the refractive index of molten Al_2O_3 in a laser-heated pendant droplet.[38] Only recently Katsumata et al. initiated electrical measurements in a TIF to measure the thermopower of molten TiO_2 using two iridium (Ir) electrodes.[39] No investigations combining electrical and chemical measurements using the pendant droplet technique have been reported.

Herein, a novel setup that combines the unique features of a pendant droplet in a TIF with three electrode measurements for studying the electrochemistry of refractory oxide melts is described. Furthermore, results from an extensive investigation of molten Al_2O_3 as an electrolyte and Ir electrodes is presented, illustrating a novel approach

*Electrochemical Society Member.
[z]E-mail: allanore@mit.edu

for thermodynamic measurements of chemical potential and entropy in refractory melts.

Experimental

Sample rod and electrode probe preparation.—Rod-shaped green bodies of samples were prepared from fine aluminum oxide powders (Al_2O_3 > 99.95% metals basis, diameter $\emptyset = 0.25$ to 0.45 μm, Alfa Aesar) placed in latex balloons (Pioneer Balloon Co.) and hydrostatically pressed at 200 MPa for 5 minutes, followed by sintering in air at 1873 K for 5 hours in a horizontal tube furnace (1725HT Furnace, CM Inc.). The sintered samples were 5 to 7 mm in diameter and 60 to 80 mm in length with a density measured by an Archimedes principle-based method[40,41] corresponding to > 90% of the theoretical density. The sintered samples were notched at one end and wound with a nichrome wire ($Ni_{60}Cr_{16}Fe_{24}$, $\emptyset = 0.45$ mm) loop for suspension from the upper furnace shaft.

Three Ir wire electrodes (Ir > 99.9%, $\emptyset = 0.5$ mm, 20 mm length, Furuya Metals Co., Ltd.) were spot-welded at their base to Ni wire leads (Ni >99.8%, $\emptyset$ 0.38 mm, Alfa Aesar), and inserted through one end of a four-bore Al_2O_3 tube (Al_2O_3 > 99.6%, $\emptyset(outer) = 6.35$ mm, AdValue Technology LLC). The Ni wire leads were extended outside of the furnace tube by securely wrapping Ni-clad copper wire (27% Ni -73% Cu, $\emptyset = 0.81$ mm, Anomet Products Inc.). No visible signs of melting or oxidation of the electrical connections were observed following operation due to the large temperature gradients present outside of the furnace hot zone (up to 200 K mm^{-1}). The bottom end of the four-bore tube was sealed with epoxy outside of the furnace. The assembled electrode probe was typically 800 mm long and at least 10 mm of Ir wire was exposed above the Al_2O_3 four-bore tube.

Electrochemical measurements.—A three-electrode configuration was employed using Ir wires for the working (WE), counter (CE) and pseudo-reference (RE) electrodes. The RE consisted of an Ir wire immersed in the molten droplet. All measured potentials are referred to this RE, unless stated otherwise. One of three geometries was employed for the WE and CE: 1) a single Ir wire with an approximate geometric surface area (A_G) of 0.07 cm^2, 2) a single Ir wire that was approximately 2 mm longer ($A_G = 0.13$ cm^2), or 3) two Ir wires TIG-welded together at their tips forming a spherical junction (approximately $\emptyset = 1$ mm, $A_G = 0.25$ cm^2).

Open circuit potential (OCP), electrochemical impedance spectroscopy (EIS), direct current (DC) linear sweep voltammetry (LSV), large amplitude Fourier transform alternating-current voltammetry (ACV) and potentiostatic and galvanostatic electrolysis measurements were performed. The details of the equipment and measurement methods are available elsewhere,[42] and only important variations are reported herein.

The cell voltage, WE potential and current were recorded during potentiostatic electrolysis experiments using a data acquisition module (DAQ, DT9837B, Data Translation, Inc.) at 36,125 Hz sampling frequency. The sinewave signal for ACV measurements was generated by a digital-to-analog function generator (DS360, Stanford Research Systems). Signal processing was performed post-recording using a code written with Scilab. The DC, 1st and higher harmonics of the current signal were obtained by inverse Fourier transform after selection of the appropriate frequency range, as presented in Reference 43. Given the nearly linear behavior of the nonfaradaic current contributions, e.g. double-layer charging, and the inherently nonlinear response of faradaic reactions, the second and higher harmonics were used to confirm the presence of faradaic reactions and determine its half-wave potential, as described in more detail in Ref. 44. The behavior of the WE at negative and positive potentials were studied in separate experiments. Additionally, during a subset of the ACV measurements, the cell voltage was simultaneously recorded. For this subset of measurements, the behavior of the WE at negative and positive potentials was studied on distinct electrodes (designated as "cathode" and "anode," resp.) within the same experiment.

DC WE and cell voltages were corrected for ohmic drop using the product of the DC current with a resistance determined as follows. The uncompensated resistance (R_u) and additional model parameters for the impedance were obtained by fitting EIS spectra to the equivalent circuit detailed in Appendix A, using ZView software (Scribner Associates, Inc). Voltammetry potential corrections for LSV and ACV required typically 80% of R_u in order to observe a monotonic variation of the DC current response with the DC potential. Cell voltage measurements was corrected using the full cell resistance (R_{cell}) obtained upon fitting the open circuit EIS spectrum. While R_u proved to decrease (−20%, typically) from open circuit values during cathodic polarization, R_{cell} only slightly changed during cell polarization (<5%). The compensated resistance (R_c) between the CE and RE ($R_c \approx R_{cell} - R_u$) was found to increase during cathodic polarization of the WE (resp. anodic polarization of the CE) in such a way as to effectively balance the decrease in R_u, therefore justifying the negligible variation in R_{cell} during open circuit and polarization measurements.

Temperature measurement.—Variation in the open circuit uncompensated resistance (R_u) with TIF lamp power (P_L) was used to evaluate temperature, as described in Appendix B using Eq. B2. At the minimum P_L required for electrode insertion into the droplet, the absolute temperature was assumed to be 2377 K, a 50 K superheat above the melting point of Al_2O_3, $T_m(Al_2O_3)$. The maximum error with respect to variation in temperature is estimated at less than 10 K, and the absolute temperature measurement error is approximately the superheat assumption, herein 50 K.

Operation.—A TIF equipped with four Xe lamps (12 kW total) and ellipsoidal mirrors, schematically shown in Figure 1, was modified for electrochemical measurements. In practice, two TIF's were employed (models FZ-T-12000-X-IV-VP and TX-12000-I-MIT-VPO-PC, Crystal Systems Corp.), which will hereafter be designated TIF I and TIF II, resp. Unless noted otherwise, the results following were obtained with TIF II. The sample rod, suspended from the upper rotating shaft, was positioned with its bottom end at the focal point of the mirrors, hereafter called "hot zone". The electrode probe was introduced through the bottom port. The vertical positions of the sample and probe were controlled independently by stepper motors with submillimeter precision. The probe and sample assembly were isolated from ambient atmosphere with a quartz tube (Technical Glass Products Inc.) sealed with Viton O-rings. A camera (EOS Rebel T5i DSLR, Canon Inc.) with a telescopic lens was employed for continuous monitoring and video recording of the sample and electrodes in the hot zone.

The inside of the quartz tube was evacuated and refilled three times with one of three gases designated "Gas A", "Gas B" and "Gas C" hereafter. Gases A and B were > 99.999% Ar and Gas C was 990 ppm O_2 with the balance Ar (UHP and certified calibration gas resp., all products Airgas Inc.). After purging, the gas flow rate was set to 50 mL min^{-1} controlled by a digital mass flow controller (FC-260V, Tylan General Inc.). The Xe lamps were powered on and P_L was gradually increased until the bottom of the rotating sample was visually molten. A stable pendant droplet formed, suspended by a balance between the melt surface tension and gravity. Rotation was halted, and the electrodes were raised upwards while monitoring the open circuit potential (E_{oc}). Visual observation and decrease in $|E_{oc}|$ ($|E_{oc}| < 5$ mV, typically) confirmed electrodes' insertion into the droplet. A trace oxygen (O_2) gas sensor (model 2001RSM, Advanced Micro Instruments Inc., sensor calibrated with air) was connected to the furnace exhaust gas for O_2 concentration quantification. At the end of the electrochemical measurements, the lamps were shut off to quench the droplet and electrodes; with cooling rates greater than 100 K s^{-1}.

Post-experimental observation and analysis.—Following experiment, the droplet and electrodes were sectioned using a diamond saw. The sections were cast in epoxy (Buehler) and fully cured. The

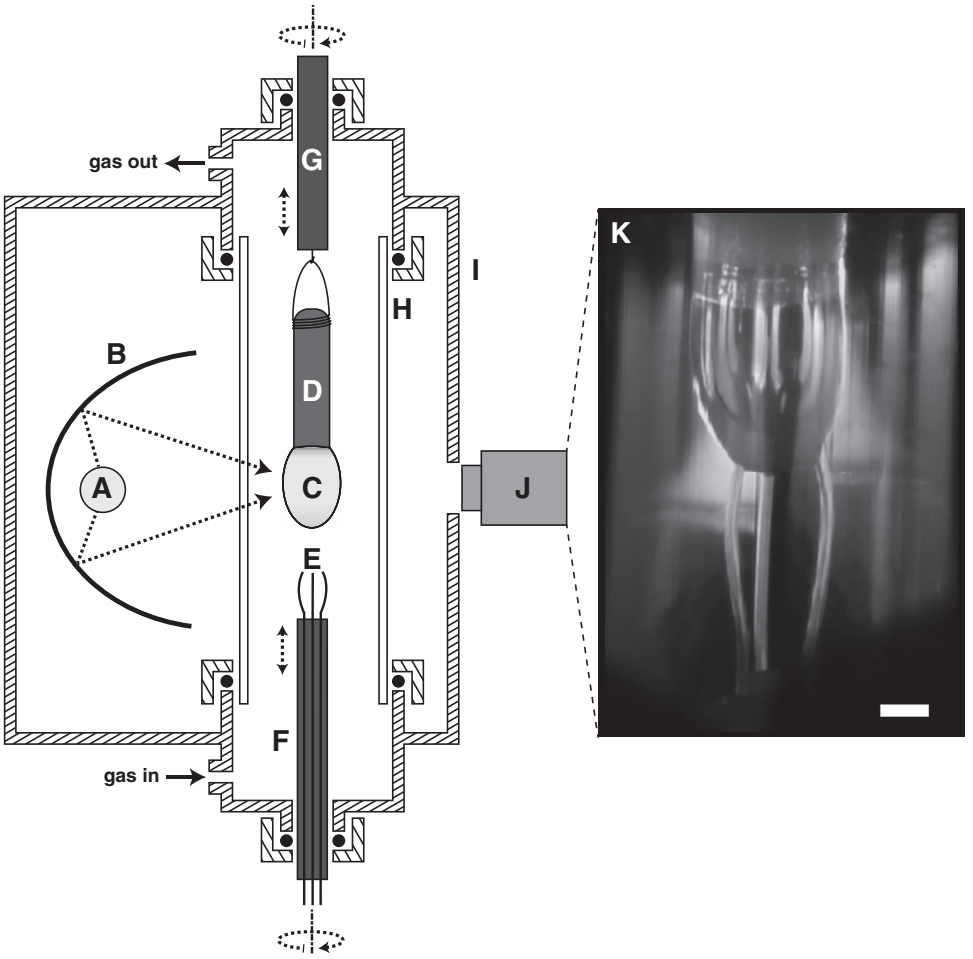

Figure 1. Schematic of the experimental setup (not to scale): (A) Xe lamp and (B) ellipsoidal mirror (one of four pairs shown), (C) molten pendant droplet (0.1 mL volume, typically) in the hot zone, (D) solid sample rod suspended by wire loop, (E) electrodes, (F) electrode leads and lower shaft, (G) upper shaft, (H) quartz tube, (I) furnace shell, (J) camera, and (K) photograph of Ir electrodes inserted into a molten Al_2O_3 droplet (scale bar 2 mm).

mounted specimens were ground with diamond abrasive pads and polished using a diamond suspension (Allied High Tech Products Inc.) down to 1 μm. Observations were made using an optical microscope and scanning electron microscope (SEM) equipped with an energy dispersive spectrometer (EDS). Further details regarding observation and analysis equipment can be found elsewhere.[42]

Results

DC and AC voltammetry.—Figure 2 shows a typical DC linear sweep voltammogram in the negative-going potential scan where the current rapidly decreases with fluctuations from the starting scan limit ($E = 1.05$ V). Very large current densities (>3.5 A cm^{-2}) are observed in this region. Further scanning toward negative potentials, a current plateau at 77 mA (label A) is observed at around $E = 0.8$ V. The current steadily decreases toward zero at open circuit ($E = 0.03$ V), close to the initial E_{oc}. On the cathodic portion of the curve ($E < 0$), the current smoothly decreases at an increasing rate (label B), until the current exhibits fluctuations (label C) at around $E = -0.3$ V. Extremely large current densities (>10 A cm^{-2}) are observed for $E < -0.4$ V.

The typical results of ACV measurements for the first ($I_{1\omega}$), second ($I_{2\omega}$) and third ($I_{3\omega}$) harmonics of the current response are shown in Figure 3. For positive potentials, a faradaic event is observed at a half-wave potential E_A^* with the characteristic peak-splitting feature across $I_{2\omega}$, $I_{3\omega}$ and higher harmonics.[45] Peak-splitting features are not clearly observed in lower harmonics possibly due to nonfaradaic contributions such as double layer charging. Gas composition was found to influence the position of E_A^*; in fact, increasing the furnace partial pressure of O_2 ($p_{O_2,furnace}$) systematically decreased E_A^*. For negative potentials, a faradaic event is observed at E_C^* with its own peaking splitting feature. The features of the shapes of the harmonic current responses for both anodic and cathodic faradaic reactions were found to be reproducible, independent of temperature and cycle number. While the peak heights in the second and third harmonic generally decreased during successive cycles at constant temperature, they remained readily distinguishable.

A summary of the measurements for E_A^* and E_C^* obtained using various experimental conditions is provided in Figure 4. Each data point corresponds to the mean of repeated measurements obtained from both positive- and negative-going scans. The error bars shown represent one standard deviation uncertainty arising from the lack of repeatability of the measured peak positions in successive cycles and scan directions. The error for R_u is estimated to be at most 10%. This corresponds to an additional error of $+/-10$ mV for the position of E_A^* and E_C^* if instrument errors in measurement of the current and voltage are neglected. Results for the parameters of linear fitting for measurements of E_A^* and E_C^* versus temperature are shown in Figure 4. Note, E_A^* was fitted with a single parameter of first-order in temperature, and E_C^* was fitted with zeroth and first-order parameters.

ACV measurements were also conducted with simultaneous cell voltage measurement. The cell voltages (U) measured at E_A^* and E_C^* are also shown in Figure 3, hereafter designated $U(E_A^*)$ and $U(E_C^*)$.

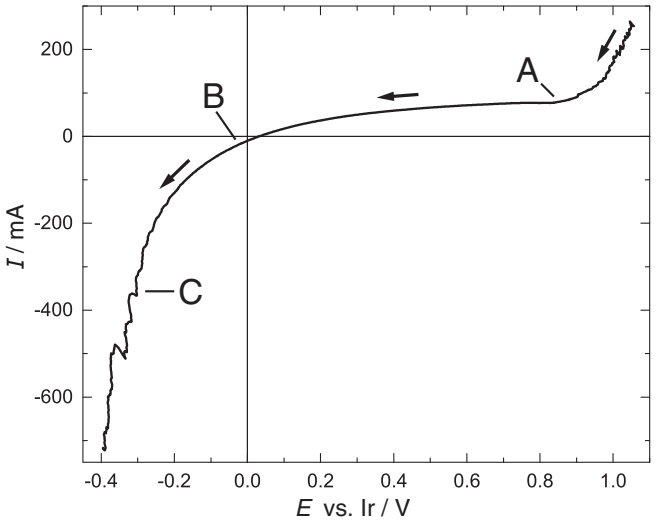

Figure 2. Typical DC voltammogram for Ir in Al_2O_3 (l) recorded in TIF I. Potential scan limits: 1.05 to −0.40 V vs. Ir, scan rate $\nu = 250$ mV s^{-1}, $T = 2377$ K, Gas B, geometric surface areas for WE ($A_{G,WE}$) and CE ($A_{G,CE}$) were approximately 0.07 and 0.13 cm^2, resp.

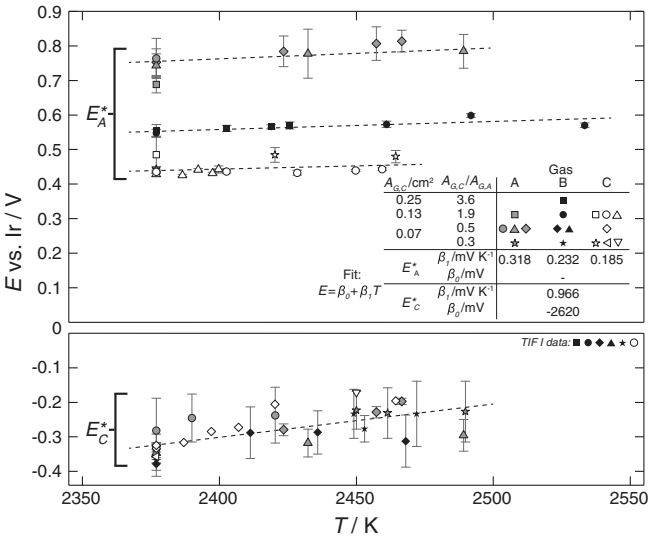

Figure 4. Variation of E_A^* (top) and E_C^* (bottom) with temperature for various electrode configurations and gas atmospheres (error bars represent 1σ uncertainty from multiple scans in both cathodic and anodic directions and lines show fitting according to $E = \beta_0 + \beta_1 T$). Note, E_A^* was fitted with a single, first-order parameter (β_1), and E_C^* was fitted with zeroth (β_0) and first-order (β_1) parameters.

The cell geometry, i.e. the cathode and anode areas ($A_{G,C}$ and $A_{G,A}$, resp.) exposed to the electrolyte, was found to influence the relative values of $U(E_A^*)$ and $U(E_C^*)$, see Appendix D for further description. In practice, it was found that $U(E_C^*)$ was systematically greater than $U(E_A^*)$, when the cathode to anode area ratio ($A_{G,C}/A_{G,A}$) was greater than 0.5 and 0.3 for Gases A and C, resp. Regardless of cell geometry, oxygen gas evolution was detected in situ by visual observation near the anode for $U > U(E_A^*)$. For the condition $U(E_C^*) > U(E_A^*)$, achieved with careful cell design, $U(E_C^*)$ will hereafter be relabeled U^o. The variation of U^o as a function of temperature for Gases A and C is presented in Figure 5. A linear unweighted fitting of all the data using an equation of the form

$$U^o = \beta_0 + \beta_1 T$$

yields $\beta_0 = 2380$ +/− 570 mV and $\beta_1 = -0.50$ +/− 0.24 mV K^{-1}.

Electrolysis.—To acquire further insight into the nature of the cathodic and anodic reactions coinciding with the faradaic events observed above, potentiostatic and galvanostatic electrolysis

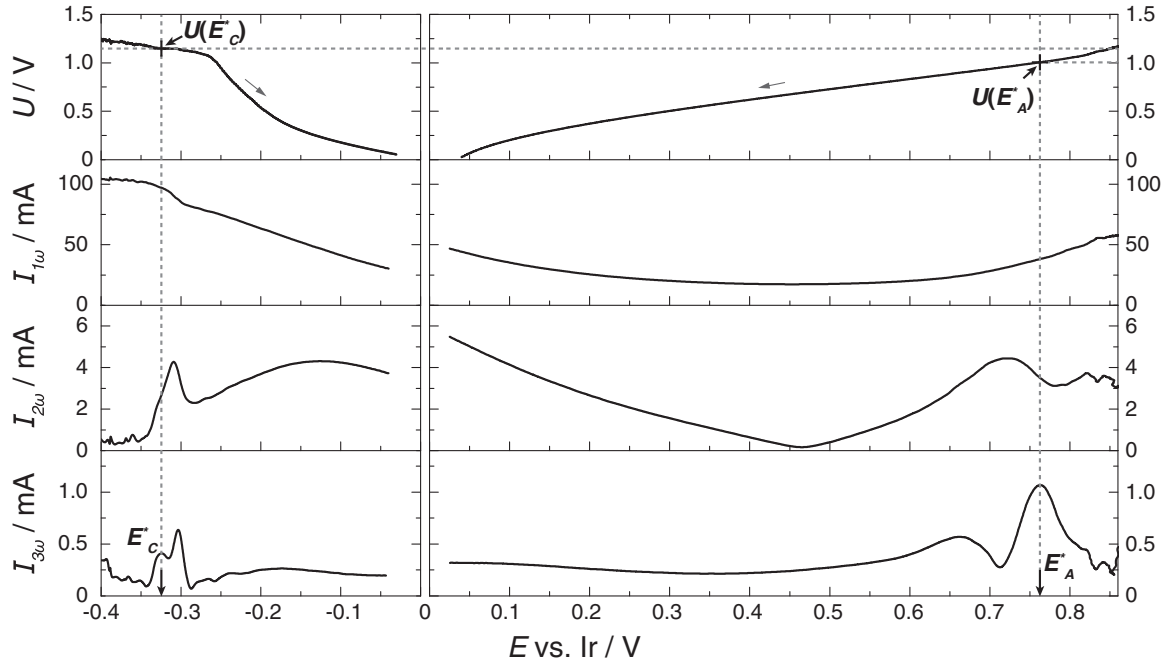

Figure 3. From top to bottom panel, DC component of cell voltage and first, second and third harmonic current responses obtained during ACV measurements. $E < 0$ corresponds to cathodic polarization study (cathode geometric surface area $A_{G,C} = 0.07$ cm^2, applied DC potential scan limits −0.55 to 0 V vs. Ir); while $E > 0$ is an anodic polarization study (anode $A_{G,A} = 0.13$ cm^2, +0.95 to 0 V vs. Ir). For both, $E_{ac} = 120$ mV, $f = 23$ Hz, $\nu = 20$ mV s^{-1}, $T = 2377$ K and Gas A. The quantities $U(E_C^*)$, E_C^*, $U(E_A^*)$ and E_A^* are defined in the text.

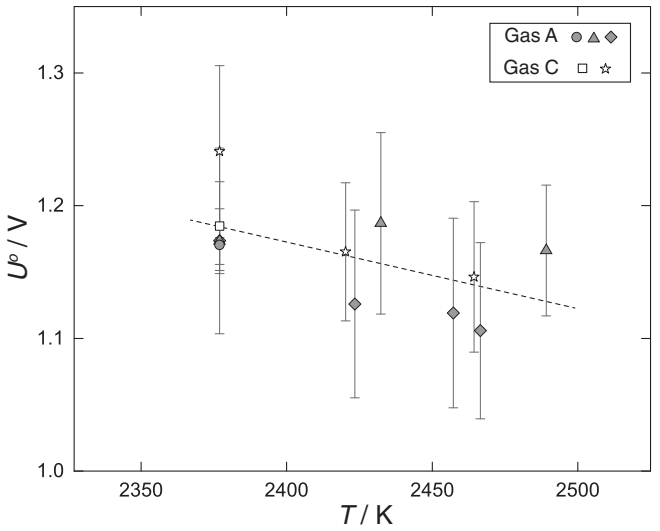

Figure 5. Variation of U^o versus temperature for Gases A and C. Linear fit of data (dashed line, $U^o = \beta_0 + \beta_1 T$) yields $\beta_0 = 2380$ +/−570 mV, $\beta_1 = -0.50$ +/−0.24 mV K^{-1}.

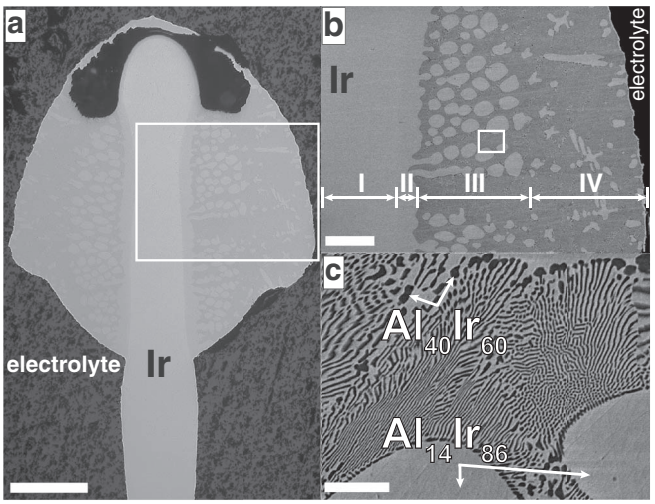

Figure 7. a. Optical micrograph of cathode cross-section after experiment shown in Figure 6b. (scale bar 300 μm). b. BSE image of boxed area in a. (scale bar 100 μm). c. High-magnification BSE image of boxed area in b. revealing the resultant solidified microstructure (scale bar 10 μm, quantitative analysis from EDS).

measurements were performed. As shown in Figure 6a, bubbling was observed perturbing the surface of the droplet above the anode when $U > U(E_A^*)$ during galvanostatic electrolysis measurements. The bubbling began immediately after applying current (typically 50 to 200 mA) to the cell. The bubbles successively emerged at a steady rate until the current was shut off, ceasing the bubbling. The O_2 gas sensor subsequently recorded a sharp increase in p_{O_2} that steadily decreased back to its initial value prior to electrolysis, a behavior similar to that reported by Allanore et al.[46] in the study of another molten oxide electrolyte. After electrolysis at moderate cell voltages (i.e. $U(E_A^*) < U < U(E_C^*)$), a droplet was quenched by turning the lamps off and the droplet and electrodes were sectioned for further analysis. Despite the presence of small ($Ø < 1$ μm) metallic particles evenly dispersed in the oxide phase, the cross-section and surface of the Ir anode remained unchanged. The Ir content in the oxide phase and Al content in the Ir cathode were both below the EDS detection limit.

Potentiostatic electrolysis measurements were also performed at high cell voltages (i.e. $U > U(E_C^*) > U(E_A^*)$) as presented in Figure 6b. For a current greater than 250 mA, gas bubbling in the vicinity of the anode and violently swirling convective currents were observed on the surface of the droplet. At very high current (>1 A), the droplet destabilized and detached from the sample rod typically after only a few seconds of current flow. For the measurements presented in Figure 6b, the droplet remained stable for the duration of electrolysis. The lamps of the TIF were shut off after 60 s, prior to the end of electrolysis, quenching the droplet and electrodes. In Figure 7a, an

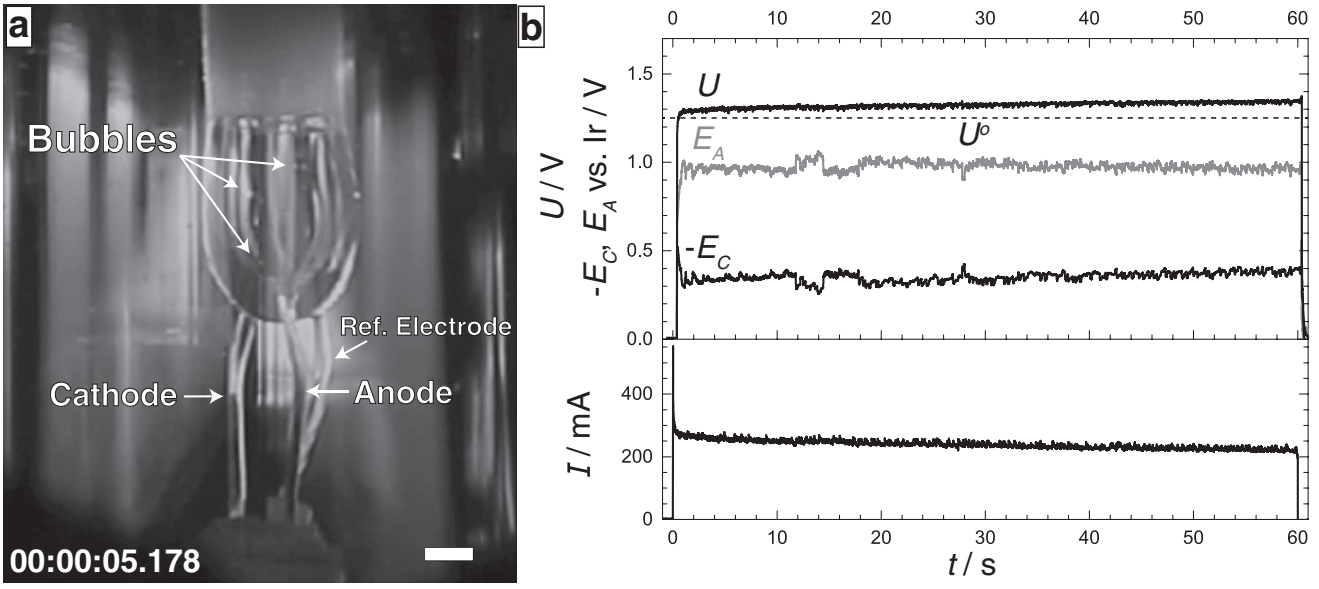

Figure 6. a. Droplet and electrodes during galvanostatic electrolysis (scale bar 2 mm). Bubbles are observed at the droplet surface near the anode (source video in supplementary materials). b. Anode (E_A) and cathode (E_C) potentials, cell voltage (U), and current (I) during potentiostatic electrolysis at 1.6 V applied cell voltage; at $t = 60$ s, the lamps were shut off ($Q = 14.32$ C, $A_{G,C} = 0.07$ cm^2, $A_{G,C} = 0.25$ cm^2, $T = 2465$ K, Gas C; source video in supplementary materials).

optical micrograph shows a cross-section of the cathode in the solidified droplet. A deposit layer is observed on the cathode at its interface with the electrolyte. The apparent volume of the cathode increased along the section of the wire wetting the molten droplet, while the anode and RE appeared unchanged. Backscattered electron (BSE) images of the cathode microstructure are shown in Figures 7b and 7c. EDS analysis for the cathode cross-section reveals that the center of the cathode (region I in Figure 7a) is nearly pure Ir with a concentration of Al below detection limit. Region II, further from the central axis of the cathode, exhibits increasing Al concentration to a maximum mole fraction $x_{Al} = 0.14$. Region III consists of round particles of an Ir-rich phase ($x_{Al} = 0.14$, $\emptyset < 75$ μm) surrounded by a lamellar two-phase structure composed of an Ir-rich phase with similar Al content and an Al-rich phase ($x_{Al} = 0.40$). A high magnification image of this region is shown in Figure 7c. Region IV contains a greater relative proportion of the lamellar two-phase field with dendritic-like structures composed of the Ir-rich phase ($x_{Al} = 0.14$). At the electrolyte-deposit interface, a thin (<5 μm) layer of the Ir-rich phase ($x_{Al} = 0.14$) is observed.

Discussion

Anode and reference electrode behavior.—The results and observations presented in Figures 2 to 4 and 6 demonstrate that the faradaic reaction measured on the anode WE at E_A^* and at a cell voltage $U(E_A^*)$ features O_2 gas evolution. In addition, the potential E_A^* proves sensitive to $p_{O_2,furnace}$. Experimental observations in this study show typically dispersed metallic particles of Ir in the melt similar to those reported in Ref. 47, but no detectable signs of Ir loss were observed both while operating Ir as an anode during bulk electrolysis or as a RE. These findings are consistent with prior thermodynamic considerations, i.e. limited solubility of IrO_x in silicates and likely presence of both IrO_x (g) and O_2 (g).[48,49] Iridium in molten Al_2O_3 is therefore hereafter considered as an inert electrode under both open circuit and anodic polarization, within the parameters and limits of detection employed in this study.

Therefore, occurring simultaneously to a cathodic reaction on the CE to be discussed later, the half-cell reaction at the WE coinciding with E_A^* is envisaged to involve oxidation of oxide ions (O^{2-}) from molten Al_2O_3 into gaseous O_2 at the furnace pressure (0.1 MPa)

$$O^{2-}\,(\text{melt}) = 2e^-\,(\text{Ir}) + \frac{1}{2}O_2\,(\text{g},\ 0.1\ \text{MPa}) \qquad [1]$$

The thermodynamic equilibrium potential for Reaction 1 is associated with inner potential ϕ_A^*, which can be defined by

$$\phi_A^* = \frac{1}{4F}\mu_{O_2}^{anode} - \frac{1}{2F}\mu_{O^{2-}}^{anode} \qquad [2]$$

where $F = 96{,}485$ C mol^{-1} and $\mu_{O^{2-}}^{anode}$ and $\mu_{O_2}^{anode}$ are the chemical potentials of O^{2-} and O_2 (g) at the anode. The standard state for O_2 (g) is chosen as pure O_2 (g) at temperature T and fugacity 0.1 MPa. Since low total pressures are encountered in this study, hereafter fugacity and partial pressure are assumed equivalent for O_2 (g), i.e. O_2 is an ideal gas and $\mu_{O_2}^{anode} = \mu_{O_2}^{o}$. The standard state for O^{2-} for $\mu_{O^{2-}}^{o}$ is defined as O^{2-} at its postulated molar concentration (85 mol L^{-1}) in pure molten Al_2O_3 at temperature T in the presence of pure O_2 (g) at 0.1 MPa. $\mu_{O^{2-}}^{anode}$ variation as a function of O^{2-} activity at the anode $a_{O^{2-}}^{anode}$ is described by

$$\mu_{O^{2-}}^{anode} = \mu_{O^{2-}}^{o} + RT\ln\left(a_{O^{2-}}^{anode}\right) \qquad [3]$$

In such conditions one can consider in more detail the overall chemical equilibria controlling the electrochemical potential E_A^* recorded versus the Ir pseudo-reference ($\phi_{ref,A}^*$) such as reported in Figure 3 where

$$E_A^* = \phi_A^* - \phi_{ref,A}^* \qquad [4]$$

Because no gas bubbles were visible on the RE electrode, the equilibria at the RE is assumed to involve O^{2-} from molten Al_2O_3 and dissolved atomic oxygen, the corresponding half-cell reaction being

$$O^{2-}\,(\text{melt}) = 2e^-\,(\text{Ir}) + O\,(\text{melt}) \qquad [5]$$

And the associated potential $\phi_{ref,A}^*$ can be defined by

$$\phi_{ref,A}^* = \frac{1}{2F}\mu_O^{ref,A} - \frac{1}{2F}\mu_{O^{2-}}^{ref,A} \qquad [6]$$

where $\mu_O^{ref,A}$ and $\mu_{O^{2-}}^{ref,A}$ are the chemical potentials of dissolved atomic oxygen and O^{2-}, respectively, at the RE, while Reaction 1 occurs at the WE. Using the same $\mu_{O^{2-}}^{o}$ defined previously for Eq. 3, enables the expression of $\mu_{O^{2-}}^{ref,A}$ variation with $a_{O^{2-}}^{ref,A}$, the O^{2-} activity at the RE. The chemical potential of dissolved atomic oxygen ($\mu_O^{ref,A}$) is assumed to be related to the equivalent partial pressure of oxygen $p_{O_2,ref}^*$ assuming equilibrium between dissolved atomic oxygen and O_2 (g) in the furnace atmosphere:

$$O\,(\text{melt}) = \frac{1}{2}O_2\,(\text{g})$$

In such conditions, $\mu_O^{ref,A}$ can be expressed as:[50]

$$\mu_O^{ref,A} = \frac{1}{2}\mu_{O_2}^{o} + \frac{RT}{2}\ln p_{O_2,ref}^* \qquad [7]$$

Combining Eqs. 6 and 7, yields the following expression for $\phi_{ref,A}^*$

$$\phi_{ref,A}^* = \frac{1}{4F}\mu_{O_2}^{o} - \frac{1}{2F}\mu_{O^{2-}}^{o} + \frac{RT}{4F}\ln\left[\frac{p_{O_2,ref}^*}{\left(a_{O^{2-}}^{ref,A}\right)^2}\right] \qquad [8]$$

E_A^* can then be related to $p_{O_2,ref}^*$ by combining Eqs. 2, 3 and 8 with 4:

$$E_A^* = \phi_A^* - \phi_{ref,A}^* = -\frac{RT}{4F}\ln\left[\left(\frac{a_{O^{2-}}^{anode}}{a_{O^{2-}}^{ref,A}}\right)^2 p_{O_2,ref}^*\right] \qquad [9]$$

Assuming the ratio of oxide ion activities $\frac{a_{O^{2-}}^{anode}}{a_{O^{2-}}^{ref,A}}$ to be unity, which seems justifiable considering Ir as an inert anode and RE and molten Al_2O_3 as an electrolyte comprised primarily of O^{2-} and aluminum ions (Al^{3+}) satisfying charge neutrality, simplifies Eq. 9 to:

$$E_A^* = -\frac{RT}{4F}\ln\left(p_{O_2,ref}^*\right) \qquad [10]$$

The single parameter fitting for E_A^* versus temperature reported in Figure 4 combined with Eq. 10 yields values of $p_{O_2,ref}^*$ for the three gas atmospheres investigated. The goodness of fit with a single first-order parameter suggests that the quantity

$$\left(\frac{a_{O^{2-}}^{anode}}{a_{O^{2-}}^{ref,A}}\right)^2 p_{O_2,ref}^*$$

is indeed invariant with temperature. Furthermore, $p_{O_2,ref}^*$ is evaluated by Eq. 10 to be 0.4, 21, and 190 Pa for Gas A ($P_{O_2,furnace}$ = 0.8 Pa, measured by trace O_2 gas sensor), Gas B ($p_{O_2,furnace}$ = 10 Pa, measured by trace O_2 gas sensor), and Gas C ($p_{O_2,furnace}$ = 990 Pa, certificate of analysis), resp. While limitations of the experimental procedure for controlling p_{O_2} at the droplet surface could at least partially explain discrepancies, the possibility of $\frac{a_{O^{2-}}^{anode}}{a_{O^{2-}}^{ref,A}}$ variation cannot be eliminated entirely. A systematic study with precise p_{O_2} control along with melt composition (i.e. basicity) variation is foreseen to provide enhanced understanding of $\frac{a_{O^{2-}}^{anode}}{a_{O^{2-}}^{ref,A}}$ and, more interestingly perhaps, oxide ion activity measurement.

Nevertheless, these observations support the validity of the assumptions for deriving Eq. 9 and, furthermore, exemplify a direct proportionality between $p_{O_2,ref}^*$ and $p_{O_2,furnace}$. The large surface

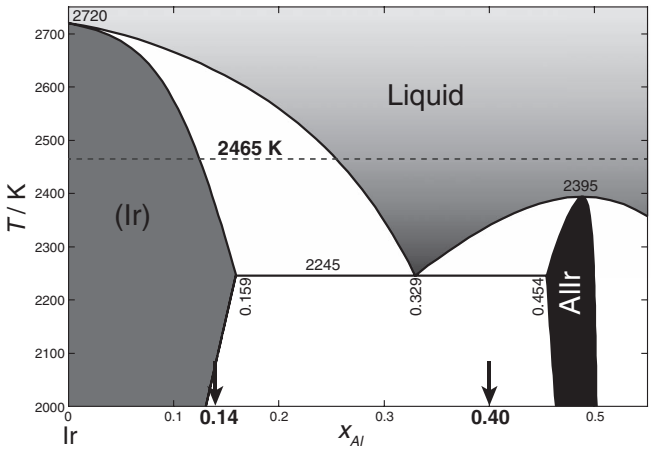

Figure 8. Ir-rich portion of the Ir-Al phase diagram calculated using FactSage[54] using the optimized parameters of Abe et al.[2] The approximate temperature during electrolysis is shown by the dashed line; arrows mark the alloy phase compositions observed upon solidification of the cathode after potentiostatic electrolysis, cf. Figures 6b–6e.

area to volume ratio of a pendant droplet justifies the rapid equilibration of oxygen species between electrodes and furnace atmosphere required for $p_{O_2,furnace}$ sensitivity. While nearby concomitant reactions occurring at the CE (cathode) or even the absence of a supporting electrolyte, i.e. electromigration effects, may limit the accuracy of the proposed interpretation, the Ir pseudo-RE is demonstrated to exhibit oxygen-electrode-like behavior. Furthermore, the results are found to be insensitive to the CE surface areas examined in this study, indicating that the current density at the CE has either negligible or exactly equivalent effect on the reactions at the WE and RE. The former is more likely given the later would require exactly reproducing the cell geometry at each measurement, which is unlikely.

All our experimental results and their interpretation, nevertheless, support that the reaction coinciding with E_A^* and $U(E_A^*)$ on an Ir anode is indeed Reaction 1. This finding provides a well-defined energy level of reference for further thermodynamic analysis of the cathode reaction, described in the following sections.

Cathode behavior.—For the cathode, the results and observations presented in Figures 2, 3, 4, 6 and 7 indicate that the faradaic reaction coinciding with E_C^* and $U(E_C^*)$, corresponds to aluminum reduction. Formation of aluminum suboxide gaseous species, e.g. AlO (g) or Al_2O (g), are thermodynamically unfavorable in the temperature range of interest and therefore need not be considered further in this discussion.[51] The electrolysis results demonstrate the reduction reaction sensitivity to the cell voltage U with respect to $U(E_C^*)$, as Al was not detected in the cathode post experiments for $U < U(E_C^*)$. Comparison with the recently assessed phase diagram for Al-Ir presented in Figure 8 indicates that the formation of a solid solution of Al in Ir at moderate concentrations (x_{Al} <0.15) is possible. Estimates of the diffusion length of Al in the solid cathode for the duration of the measurements (60 s) suggest that Al will not diffuse far into the Ir cathode (<5 μm).[52] On the other hand for $U > U(E_C^*)$, the post-quenched cathode contained Al-Ir alloy phases and a morphology comprised of fine lamellae and dendrites indicative of a rapidly solidified liquid, as exemplified in Figure 7. Comparison with Figure 8 confirms the formation of a liquid given the operating temperature ($T \approx 2485$ K) for the phase compositions observed by EDS ($x_{Al} = 0.14$ and 0.40). The discrepancy between the measured composition of the Al-rich phase ($x_{Al} = 0.40$) and that of the minimum solubility limit for the $AlIr_X$ intermetallic compound from Abe et al.[2] ($x_{Al} = 0.454$) is presumably due to the fine microstructure (<1 μm) and spatial resolution limits of the analytical technique (EDS, 1 μm, approx.). E_C^* and $U(E_C^*)$ are then hypothesized to coincide with the reduction of Al^{3+} leading to the formation of liquid Al-Ir metal alloy on the Ir cathode

$$Al^{3+}\,(melt) + 3e^-\,(Ir) = Al\,(l, Ir) \qquad [11]$$

At isothermal conditions in the measured temperature range (T = 2377 to 2489 K), the liquid metal formation on the Ir cathode at equilibrium conditions (see Figure 8) coincides with the two-phase (liquid and fcc solid solution) region in the Ir-rich portion of the Al-Ir system. For interpretation of E_C^* and $U(E_C^*)$ measurements, E_C^* can be expressed as

$$E_C^* = \phi_C^* - \phi_{ref,C}^*$$

where ϕ_C^* and $\phi_{ref,C}^*$ are respectively the cathode and RE inner potentials during E_C^* measurement. The latter is not necessarily the same as $\phi_{ref,A}^*$ for E_A^* measurements. For $E < E_C^*$, current densities significantly larger than that observed during O_2 gas evolution at and beyond E_A^* were measured, viz. comparing Figures 2 and 3. Such difference in magnitude of current density (6000 mA cm^{-2} vs. 1200 mA cm^{-2}, approx.) shares a candid agreement with the physical nature of the liquid-liquid versus liquid-gas reactions coinciding with E_C^* and E_A^*, resp. However, like for E_A^*, the CE (anode) surface area had negligible influence on E_C^*, as presented in Figure 4.

Although derivation of a model for the fitting parameters of E_C^* is possible, the discussion of the physical significance of β_0 and β_1 will be limited here due to the indefinite nature of the Ir pseudo-reference electrode. The parameter β_0 is associated with the enthalpy change accompanying aluminum reduction, for which the large negative value ($\beta_0 = -2.62$ V) agrees with tabulated data[2,53,54] at least in sign and order of magnitude. On the other hand, β_1 is related to the entropy change accompanying aluminum reduction and entropy of oxygen at the RE, and a similar agreement is observed for its value ($\beta_1 = 0.966$ mV K^{-1}). In contrast to E_A^*, the results for E_C^* do not exhibit clear dependence on $p_{O_2,furnace}$, as shown in Figure 4. This observation suggests that Al (l,Ir) formation at the cathode influences the potential of the reference electrode ϕ_{ref}. Assuming Reaction 5 describes ϕ_{ref} and charge neutrality again limits Al^{3+} and O^{2-} activity variation, a reduction in oxygen potential at the RE (i.e. $p_{O_2,ref}$) is concluded to accompany formation of Al (l,Ir) at the cathode. This phenomenon is hypothesized to occur when Al (l,Ir) is transported from the cathode to be oxidized by dissolved atomic oxygen in the RE vicinity more rapidly than oxygen can be replenished from the anode or furnace atmosphere.

Nevertheless, all our observations and experimental results further support the connection between Reaction 11 and E_C^* and $U(E_C^*)$.

Significance of U^o and thermodynamic analysis.—Given the preceding discussion on E_A^* and E_C^*, the definition of U^o can be revisited and its significance discussed. Formally, U^o was defined as the value of $U(E_C^*)$ that satisfies $U(E_C^*) > U(E_A^*)$. Under such conditions, the required current density driving O_2 gas evolution via Reaction 1 on the anode must have been achieved during measurement of $U(E_C^*)$ coinciding with Reaction 11. Figure 9 is a schematic illustration of the

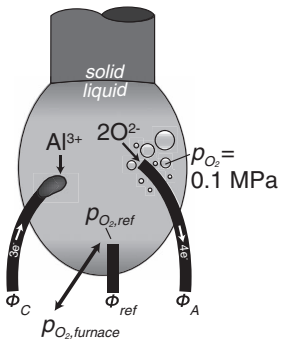

Figure 9. Electrochemical situation for the droplet and electrodes during cell polarization $U > U(E_C^*) > U(E_A^*)$. ϕ_C, ϕ_{ref} and ϕ_A are the inner electric potentials of the cathode, RE and anode, resp. Details described in text.

corresponding electrochemical configuration for $U > U(E_C^*) > U(E_A^*)$. Since $U^o = U(E_C^*)$, the postulated state of Al is well defined (see previous section). What remains is a question regarding the state of O_2 (g) at the anode. For bubble formation to occur, neglecting the vapor pressure of species other than O_2 (g), mechanical equilibrium requires that the internal bubble pressure exerted by p_{O_2} at least balances the total external pressure (p_{ext}) exerted on the Al_2O_3 droplet by the furnace gas, i.e. $p_{ext} = 0.1$ MPa. Assuming zero contact angle, the maximum pressure of O_2 (g) is estimated from the Young-Laplace expression

$$p_{O_2,max} = p_{ext} + \frac{2\gamma}{r} \quad [12]$$

where r and γ are the bubble's radius and surface tension, resp. The relative difference of O_2 (g) chemical potential μ_{O_2} and standard state $\mu^o_{O_2}$ with respect to variation in p_{O_2} is

$$\frac{\mu_{O_2} - \mu^o_{O_2}}{|\mu^o_{O_2}|} = \frac{RT}{|\mu^o_{O_2}|} ln\left(p_{O_2}\right) \quad [13]$$

At the surface of the droplet, the observed O_2 (g) bubble radii (r) are of the order 250 μm and the surface tension γ of molten Al_2O_3 was previously measured to be approximately 650 mN m^{-1}.[27] Combining these values with Eqs. 12 and 13 and tabulated data for $\mu^o_{O_2}$,[53] μ_{O_2} differs from $\mu^o_{O_2}$ by less than 1%. This remains valid even if the radii of the bubbles were an order of magnitude smaller at the surface of the droplet, i.e. detached bubbles coalesce and grow after leaving the anode surface. Thus, a reasonable assumption is that the energy of O_2 at the anode surface is essentially fixed at the standard state energy $\mu^o_{O_2}$ for $U > U(E_A^*)$ and $p_{ext} = 0.1$ MPa.

Therefore, U^o is the thermodynamic minimum decomposition potential difference, the minimum electrical work, to drive the overall cell reaction

$$Al_2O_3\,(l) \rightarrow 2\,Al\,(l, Ir) + 1.5\,O_2\,(g, 0.1\,MPa)$$

with a corresponding Gibbs energy of reaction per mole Al_2O_3 computed via

$$\Delta_r G = 6FU^o = 2\,\mu_{Al(l,Ir)} + 1.5\,\mu^o_{O_2} - \mu^o_{Al_2O_3} \quad [14]$$

where $\mu^o_{O_2}$ and $\mu^o_{Al_2O_3}$ are the standard chemical potentials of O_2 (g) (standard state defined previously) and Al_2O_3 (l) (standard state pure liquid, T and $p = 0.1$ MPa), resp. and $\mu_{Al(l,Ir)}$, or simply μ_{Al}, is the chemical potential of Al in the two-phase region solid-solution and liquid. Using tabulated data for $\mu^o_{O_2}$ [53] and $\mu^o_{Al_2O_3}$ [54] and measured values for U^o shown in Figure 5, μ_{Al} is determined from the resulting expression derived from Eq. 14

$$\mu_{Al} = 3FU^o + 0.5\mu^o_{Al_2O_3} - 0.75\,\mu^o_{O_2} \quad [15]$$

The results for μ_{Al} using Eq. 15 are plotted versus temperature in Figure 10. For comparison, the chemical potential of Al for the liquid and fcc solid solution phase equilibrium in the Ir-rich portion of the binary Al-Ir system was also calculated using FactSage.[51] Model parameters for this binary equilibrium are from the most recent Al-Ir thermodynamic assessment.[2] The fit of measured values for μ_{Al}, averaging −285.4 kJ mol^{-1} for the measured temperature range (T = 2377 to 2489 K), is less than 7% greater than those calculated using FactSage. Furthermore, the average entropy $S_{Al,avg}$ for the same temperature range is 114.4 J mol^{-1} K^{-1} which despite a large error (+/−60%) is also in close agreement. As pointed out by Abe et al., no experimental data for the liquid phase was available, and the Gibbs energy model for the liquid phase was fit to available data for the eutectic phase boundary (T = 2245 K) while maintaining ideal entropy of mixing. Given these circumstances, the agreement is remarkable and further supports the validity of the approach and postulated descriptions for Reaction 1, E_A^* and $U(E_A^*)$ as well as Reaction 11, E_C^* and $U(E_C^*)$.

Since entropy is proportional to the first derivative of U^o with respect to temperature, errors in the independent measures of the variation of U^o and T are the two most important factors in determining

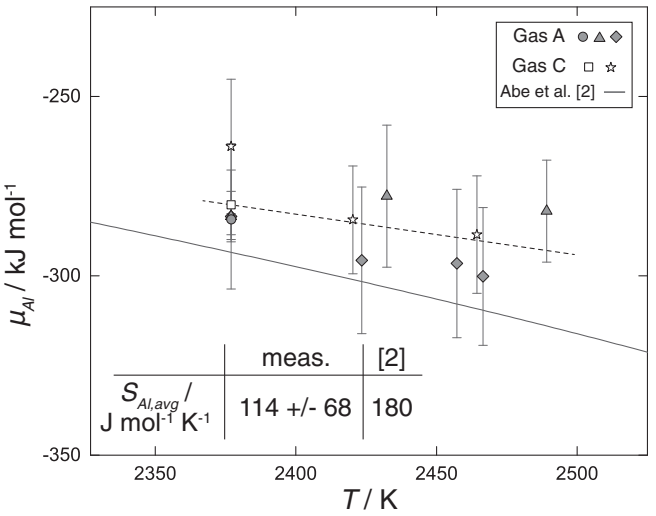

Figure 10. Variation versus temperature of the measured chemical potential (μ_{Al}) and average partial molar entropy (S_{Al}) of Al at the solid-liquid phase boundary of the Ir-rich portion of the phase diagram; linear fit (dashed line). Shown for comparison are those values calculated from the recent thermodynamic assessment.[2]

the accuracy for entropy measurements with the proposed approach. The remarkable sensitivity to changes in U^o with temperature variations has been demonstrated by the results presented in Figure 5. Measurements of U^o were repeatable within 5% on average. Furthermore, these values were measured with a precision of around 1 mV. Clearly, the method employed for temperature measurement in this investigation could be refined (see Appendix B). Although, the sensitivity of the impedance-based temperature measurement to temperature change within the same experiment was quite good (error <10 K); the absolute temperature, used to anchor an experimental dataset, could be determined only within an estimated accuracy of +/−50 K. The latter uncertainty was responsible for the relatively large error on $S_{Al,avg}$. The accuracy of the approach for entropy measurements would therefore benefit from of a secondary means of measuring temperature in situ. Enhancing the accuracy in E_C^* evaluation and the interpretation of the AC current harmonics also calls for development of an electrochemical theory for ACV involving metal deposition on a non-inert substrate.

Conclusions

A containerless, pendant droplet technique utilizing a TIF and electrodes for electrochemical study of refractory oxide melts was described. For the first time, the direct electrolytic decomposition of molten Al_2O_3 to O_2 gas and Al metal (alloyed with Ir) was observed, confirming the ionic nature of molten Al_2O_3. The reactions corresponding to oxygen evolution and Al deposition from a single-component electrolyte (Al_2O_3) on an Ir electrode were systematically investigated. The decomposition voltage of molten Al_2O_3 was measured with high precision using ACV, and the results demonstrated remarkable sensitivity to temperature enabling measurement of Gibbs energy and entropy without the use of a membrane. The chemical potential and entropy of Al in the liquid Al-Ir alloy at the Ir-rich solid-liquid phase boundary was measured for the first time. These results were in remarkably close agreement with the most recent thermodynamic assessment of the Al-Ir system. A significant error for entropy (+/−60%) persisted due to error in determining absolute temperature. Nevertheless, these results have illustrated a viable pathway for measuring chemical potential and entropy at UHT in refractory melts by combining the enhanced sensitivity of ACV and flexibility of containerless processing by pendant droplet technique.

Acknowledgments

The authors thank Dr. Guillaume Lambotte and Ms. Sara Warkander for their pioneering effort to implement electrochemical measurements in the TIF furnace. The authors also gratefully wish to acknowledge contributions from Ms. Melody Wang, Mr. Erick I. Hernandez and Prof. Joseph Checkelski. This research was funded by the US Office of Naval Research (ONR) under grant Contract # N00014-11-1-0657.

Appendix A

Impedance measurements.—A typical open-circuit Nyquist plot is shown in Figure A1. The magnitude of the impedance $|Z|$ decreases with decreasing frequency $f = 200$ kHz to 15 kHz with little variation in the real component of impedance Z_{Re}, attendant behavior of the electrode lead inductance. At around $f = 15$ kHz, the impedance crosses a point in which the imaginary component of impedance Z_{Im} is zero, the marked "X" in Figure A1. As f is further decreased from 15 kHz to 5 Hz, $|Z|$ continues to increase with an approximately unity slope. At low frequencies, $|Z|$ approaches an asymptotic value and Z_{Im} approaches zero.

A model of the equivalent circuit (also shown in Figure A1) was used to fit the data and estimate values for the circuit elements. The external inductance L_{ext} was estimated by a separate measurement of the impedance of the shorted leads in the TIG-welded electrode configuration and was arbitrarily fixed during the fitting along with the charge transfer resistance R_{ct}, which was taken as a negligibly small value (10^{-8} ohms). This is a reasonable assumption given the UHT's and relatively fast kinetics anticipated for the faradaic reaction controlling the impedance at open circuit. A generalized finite Warburg element (GFW) was taken as the element descriptive of mass transfer of the electroactive species. The GFW impedance (Z_W) is given by[55]

$$Z_W = R_W \frac{\tanh[(iT_W\omega)^{P_W}]}{(iT_W\omega)^{P_W}}$$

where $\omega = 2\pi f$, $i = \sqrt{-1}$, and R_W, T_W and P_W are fitting parameters. The results for R_u, C_{dl}, R_W, T_W and P_W are presented in Table AI. Temperature was estimated based upon variations of R_u with P_L (as described in Appendix B).

Appendix B

Temperature measurement.—Temperature (T) was evaluated from changes to the solution resistance with lamp power (P_L). The solution resistance (R_s) can be calculated by

$$R_s = R_u - R_{ext}$$

where R_u is the uncompensated resistance evaluated from open circuit EIS measurements, and R_{ext} is the external resistance between the Ir electrode-electrolyte interface and potentiostat. R_{ext} was determined as a function of P_L by measuring the impedance of the shorted loop in the TIG-welded electrode configuration. R_{ext} was found to be a weakly increasing function of P_L, which is expected of a metallic conductor. The relation between R_s and conductivity (σ) of the electrolyte is given by

$$R_s = \frac{G}{\sigma}$$

where the geometric factor (G) depends upon factors such as electrode configuration in the droplet and droplet size. Assuming σ obeys an Arrhenius dependence with respect to temperature, then

$$\sigma = \sigma_0 \exp(-E_\sigma / k_B T) \qquad [B1]$$

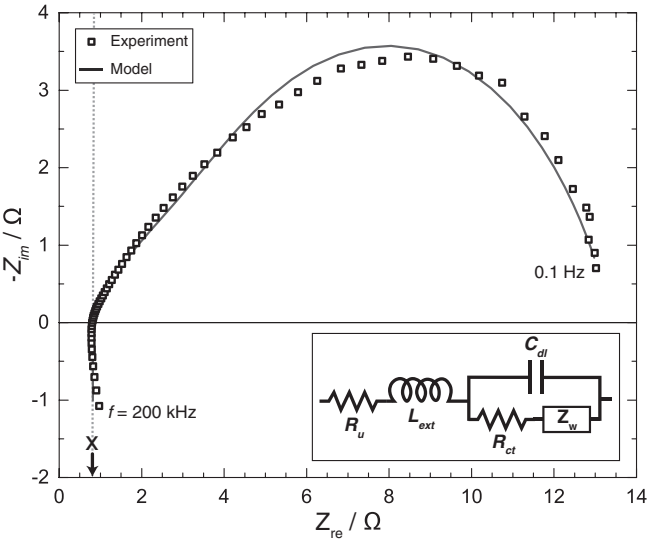

Figure A1. Impedance spectrum recorded at open circuit. The experimental data points are shown along with the model fit. Model parameters are reported in Table AI. $E_{ac} = 10$ mV, $f = 200$ kHz to 0.1 Hz with 10 points per decade, $P_L = 55\%$, Gas C, and $A_{G,WE} = 0.07$ cm^2 and $A_{G,CE} = 0.13$ cm^2, approx. TIF I was employed to obtain the data shown here.

where σ_0 is the Arrhenius pre-exponential factor, E_σ is the activation energy of conductivity and k_B is the Boltzmann constant. If E_σ and σ_0 are assumed to be constants in the temperature range of interest, then the following relation applies

$$T = \left[\frac{1}{T_0} + \frac{k_B}{E_\sigma}\left\{\ln\left(\frac{G_o}{G}\right) + \ln\left(\frac{R_s}{R_{s,0}}\right)\right\}\right]^{-1} \qquad [B2]$$

which connects R_s measured at an unknown T and the solution resistance ($R_{s,0}$) measured at a reference temperature (T_0). Several workers reported measurements of σ for Al_2O_3 (l) as a function of T in the literature.[21,56–63] A critical assessment of these results in the temperature range $T_m(Al_2O_3) = 2327$ K[64,65] to $T_m(Ir) = 2719$ K[65,66] is provided in Appendix C, yielding $E_\sigma = 1.67 +/-0.15$ eV. At the minimum P_L required for electrode insertion into the droplet, this condition is assigned the temperature $T_0 = 2377$ K, a 50 K superheat above $T_m(Al_2O_3)$. The error associated with T_0 is estimated to be 50 K. This assumption is expected to be reasonable considering the vicinity of the droplet to the solid-liquid interface and temperature measurements during other experiments with a nearby thermocouple.

Taking geometric effects into account, the perpendicular distance between wires in the droplet varies by a negligible amount over the course of an experiment, so only the effective area (A_e) described by an effective radius (r_e) can influence G, and the following approximate relation applies

$$\frac{G_o}{G} \approx \frac{A_e}{A_{e,o}} \approx \left(\frac{r_e}{r_{e,o}}\right)^2$$

Where G_o, $A_{e,o}$ and $r_{e,o}$ are the geometric constant, effective area and radius, resp., at the reference temperature T_o. Assuming the behavior of r_e varies similarly to the droplet radius (r) and only moderate changes to P_L ($\Delta P_L = P_L - P_{L,o}$ <5% for lamp power $P_{L,o}$

Table AI. EIS Fitting Parameters TIF I was employed to obtain the data shown here.

Gas	LP/%	L_{ext}*/μH	R_{ct}*/10^{-8} ohm	R_u/10^{-3} ohm	C_{dl}/ μH	R_W/ ohm	T_W/10^{-3} sec	P_W/ 10^{-3}
B	56	0.8	1	704	396 (36)	5.7 (0.1)	330 (30)	355 (6)
	57			691 (6)	404 (38)	5.5 (0.1)	340 (30)	404 (6)
	58			678 (6)	435 (43)	5.0 (0.1)	350 (30)	435 (6)
	59			674 (6)	454 (44)	4.7 (0.1)	370 (30)	454 (5)
C	55	0.8	1	814 (6)	154 (8)	12.6 (0.1)	280 (10)	371 (4)
	56			794 (6)	170 (9)	10.7 (0.1)	260 (10)	370 (4)
	57			772 (5)	197 (11)	9.5 (0.1)	260 (10)	368 (4)
	58			753 (5)	225 (13)	8.5 (0.1)	260 (10)	367 (4)
	59			743 (5)	252 (15)	7.6 (0.1)	260 (10)	366 (4)

*Arbitrarily fixed parameters, required for least-squares fitting convergence.

at T_o), the Taylor series expansion applies (neglecting second and higher order terms)

$$\frac{r_e}{r_{e,o}} \sim 1 + \frac{1}{r_o}\frac{dr}{dP_L}\Delta P_L$$

where r_o is the droplet radius at T_o. By comparing images of the droplet at various lamp powers with image analysis software, the approximate relation $\frac{1}{r_o}\frac{dr}{dP_L} = \frac{0.02}{P_L}$ was determined valid for all experiments.

Considering only errors associated with E_σ and T_0 and neglecting all other contributions, the error with respect to measurement of the variation in temperature within the same experiment is less than 10 K. However, as decribed earlier, the error for absolute temperature is estimated to be 50 K.

Appendix C

Assessment of Al_2O_3 conductivity.—Previous efforts to measure the electrical conductivity of Al_2O_3 (l) are numerous,[21,56–63] which is uncommon for refractory melts. Although recent researchers have compared their results with a partial selection of previous efforts, the last complete review of Al_2O_3 (l) conductivity is that of Shpil'rain et al.[60] More recent reviews, e.g.,[67] have omitted without justification contributions from the aerodynamic levitation method.[21,61,62] Thus, an updated review of Al_2O_3 (l) conductivity is prudent. Substantial disagreement exists, given the errors reported, along with the effect of atmosphere (oxygen potential). The atmosphere employed is noted where possible, but its effect is neglected in the current assessment. Careful study of the effect of impurities and atmosphere (oxygen potential) would help resolve the discrepancies. A summary of previous measurements and the results of this assessment in the temperature range range $T_m(Al_2O_3) = 2327$ K[64,65] to $T_m(Ir) = 2719$ K[65,66] are presented in Figure C1.

Van Arkel et al.[56] were the first to report the conductivity of Al_2O_3 (l). Their estimate, 15 S cm^{-1}, was derived indirectly from the performance of an electric arc above Al_2O_3 (l) in an electric arc furnace. They assigned an error of at least 50% owing to the approximate nature of their calculations. For this reason, this result was not included in this assessment.

Fay[57] reported conductivity at 2400 K to be 3.84 S cm^{-1} with an estimated error of 5% using the two concentric electrode technique with an Ir electrode and crucible. The atmosphere was air, but the heat source was an oxygen-hydrogen flame that Fay conceded likely made the atmosphere reducing. Temperature was measured with an optical pyrometer pointed at the melt, but the author assumed unity emittance, so $T = 2400$ K represents a slight underestimate of the actual temperature.

Elyutin et al.[58] used the two electrode technique with induction heating from $T = T_m(Al_2O_3)$ to 2800 K. They found that conductivity varied from 0.71 S cm^{-1} at 2325 K to 1.26 S cm^{-1} at 2775 K with 11% estimated error. At the same temperatures, they reported, for the first time, the activation energy varied from $E_\sigma = 0.89$ eV to 0.60 eV. Helium and vacuum atmospheres were used with no apparent effect on conductivity.

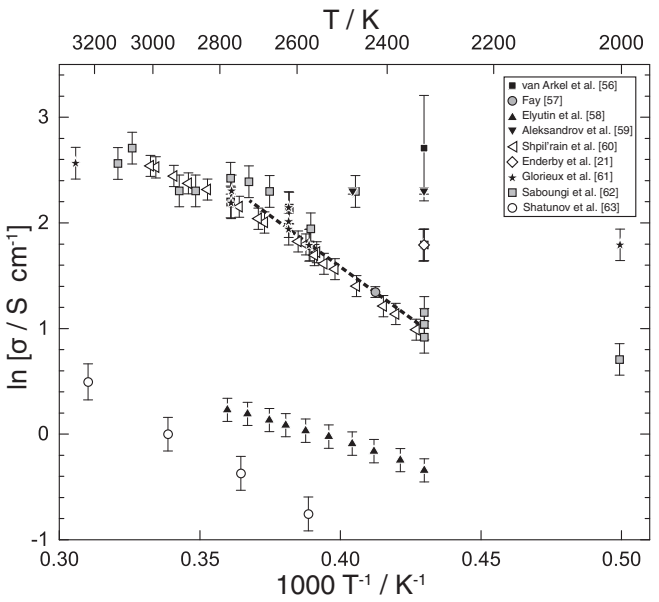

Figure C1. Arrhenius plot comparing previously reported conductivity measurements for Al_2O_3 (l). Comparing the fit (dashed line, see text for details) with Eq. B1, the activation energy of conductivity E_σ and Arrhenius pre-exponential factor σ_0 were found to be 1.67 +/−0.15 eV and 11 +/−8 kS cm^{-1}, resp. for the temperature range $T_m(Al_2O_3) = 2327$ K[64,65] to $T_m(Ir) = 2719$ K.[65,66]

Later, Shpil'rain et al. first questioned the induction heater's electromagnetic field on the results, which might at least partially explain why Elyutin et al.'s results are an order of magnitude lower the other reports. For these reasons, these results were not included in this assessment.

Aleksandrov et al.[59] used the two electrode method with an inductively-heated cold crucible from $T = T_m(Al_2O_3)$ to 2473 K. They measured 10 S cm^{-1} with a reported error of 3% and no temperature dependency. The atmosphere was air. Later, Shpil'rain et al.[60] suggested that the error was probably much greater than this given the significant temperature gradients likely present in the melt. For this reason, this result was not included in this assessment.

Shpil'rain et al.[60] used the two concentric electrode technique from $T = T_m(Al_2O_3)$ to 3000 K with an estimated error of 10%. The atmosphere was either pure Ar or vacuum, and conductivity was exactly the same in both atmospheres. Mo and W electrodes were employed with Mo and W crucibles, resp. Temperature was measured by an optical pyrometer using a black body cavity in the crucibles. They reported E_σ varied from 1.85 eV at 2400 K to 0.93 eV at 3000 K.

Enderby et al.[21] measured conductivity at a single temperature near $T_m(Al_2O_3)$ to be 6 S cm^{-1} with 15% error using the contactless radio frequency resonator technique (RFR) coupled with aerodynamic levitation. The atmospheric composition was not reported. A pyrometer is shown in the schematic of the setup, but no temperature was reported. Glorieux et al. and Saboungi et al. report suspiciously similar values at the $T_m(Al_2O_3)$. However, since no temperature was reported in Ref. 21, this common value from Refs. 21, 61, 62 was not included in this assessment.

Continuing measurements by contactless RFR coupled with aerodynamic levitation, Glorieux et al.[61] reported measurements extending from under-cooled liquid at $T = 2000$ K to 3300 K with an estimated accuracy of 15%. Here, they calibrated a pyrometer for temperature measurement using the thermal arrest upon melting. They mentioned that Ar and O_2 gas compositions were used, but do not specify which data points correspond to which gas environments.

Further continuing measurements by contactless RFR coupled with aerodynamic levitation, Saboungi et al.[62] report the conductivity as a function of temperature with an error of 15%. They mention that the levitation gas composition had an influence on the conductivity. However, the exact numerical change in conductivity, nor the atmospheric compositions (presumably Ar and O_2 as reported in Ref. 61) used during measurements were reported. No effort was made to explain the details for temperature measurement (emittance, etc.), but it can be assumed they calibrated the pyrometer using melting thermal arrest as described in Ref. 61.

More recently, Shatunov et al.[63] reported conductivity by energy balance considerations using an induction-heated cold crucible in air. They reported 0.47 to 1.64 S cm^{-1} with 17% estimated error for $T = 2573$ to 3223 K. Their results are substantially lower than that of all previous measurements, which they attributed to impurities and atmosphere (oxygen potential). Given the significant difference from previous reports, the validity of this justification requires more evidence. They did not report the purity of the samples used in their experiments, nor the method of pyrometer calibration. Additionally, temperature appears to have been measured only at the top surface of melt. Furthermore, given the indirect nature of the methodology, this approach measures an effective conductivity for the entire crucible charge, in which substantial temperature gradients were present (>100 K cm^{-1}). No effort was made to explain the contribution of this effect on their results. For these reasons, the single data point in the desired temperature range was not included in this assessment.

Appendix D

Influence of cell geometry on U_A^* and U_C^*.—The DC current (I) is related to the DC current density (j) by the electroactive surface area (A) according to

$$I = Aj \qquad [D1]$$

Assuming that the cell voltage (U) is a monotonically increasing function of I, then the condition for $U^o \equiv U(E_C^*)$, i.e. $U(E_C^*) > U(E_A^*)$, can be rewritten as

$$I\left(E_C^*\right) > I\left(E_A^*\right) \qquad [D2]$$

where $I(E_C^*)$ and $(I(E_A^*)$ are the DC current magnitudes occurring at $U = U(E_C^*)$ and $U = U(E_A^*)$, resp. Substituting Eq. D1 into D2,

$$A_C\, j\left(E_C^*\right) > A_A\, j\left(E_A^*\right) \qquad [D3]$$

Where A_C (A_A) is the cathode (anode) electroactive surface area and $j(E_C^*)$ ($j(E_A^*)$) is the DC current density magnitude at the cathode (anode) concomitant with potential E_C^* (E_A^*). Rearranging D3, and assuming $\frac{A_C}{A_A} = \frac{A_{G,C}}{A_{G,A}}$ yields

$$\frac{A_{G,C}}{A_{G,A}} > \frac{j\left(E_A^*\right)}{j\left(E_C^*\right)} \qquad [D4]$$

In practice, Eq. D4 was satisfied for $\frac{A_{G,C}}{A_{G,A}} > 0.5$ and 0.3 for Gases A and C, resp.

List of Symbols

Symbol	Name	SI unit or value
a_i	activity of species i	
A	area	m^2
A_G	geometric surface area	m^2
C_{dl}	double-layer capacitance	F
E	electrode potential	V
E_A (E_C)	anode (cathode) potential	V
E_{ac}	applied potential AC amplitude	V
E_{oc}	open circuit potential	V
E_σ	Arrhenius activation energy of conductivity	eV
f	frequency	Hz
F	Faraday constant	96,485 C mol^{-1}
$\Delta_r G$	reaction Gibbs energy	J mol^{-1}
G	geometric factor	m^{-1}
i	imaginary unit	$\sqrt{-1}$
I	electric current	A
$I_{n\omega}$	n^{th} harmonic of electric current	A
j	electric current density	A m^{-2}
k_B	Boltzmann constant	8.617 eV K^{-1}
L_{ext}	external inductance	H
p	pressure	Pa
p_i	partial pressure of species i	Pa
P_L	relative lamp power	%
P_W	generalized finite Warburg element (GFW) fitting parameter	
Q	electric charge	C
r	radius	m
R	gas constant	8.314 J mol^{-1} K^{-1}
R_c	compensated resistance	Ω
R_{ct}	charge transfer resistance	Ω
R_{cell}	cell resistance	Ω
R_{ext}	external resistance	
R_s	solution resistance	Ω
R_u	uncompensated resistance	Ω
R_W	GFW fitting parameter	Ω
S	entropy	J K^{-1}
S_i	partial molar entropy	J mol^{-1} K^{-1}
t	time	s
T	temperature	K
T_m	melting point	K
T_W	GFW fitting parameter	s
U	cell voltage	V
x_i	mole fraction of species i	
Z	impedance	Ω
Z_{im}	imaginary component of impedance	Ω
Z_{re}	real component of impedance	Ω

Greek

β_n	fitting parameter of order n	varies
$Ø$	diameter	m
γ	surface tension	N m^{-1}
μ_i	chemical potential	J mol^{-1}
μ_i^o	standard chemical potential	J mol^{-1}
ν	potential scan rate	V s^{-1}
ω	angular frequency	rad s^{-1}
ϕ	inner electric potential	V
σ	conductivity	S m^{-1}
σ_o	Arrehnius pre-exponential factor of conductivity	S m^{-1}

References

1. J. Sato, T. Omori, K. Oikawa, I. Ohnuma, R. Kainuma, and K. Ishida, "Cobalt-base high-temperature alloys," *Science*, **312**(5770), 90 (2006).
2. T. Abe, C. Kocer, M. Ode, H. Murakami, Y. Yamabe-Mitarai, K. Hashimoto, and H. Onodera, "Thermodynamic re-assessment of the Al-Ir system," *Calphad*, **32**(4), 686 (2008).
3. A. Allanore, "Features and challenges of molten oxide electrolytes for metal extraction," *J. Electrochem. Soc.*, **162**(1), 13 (2014).
4. M. Zinkevich, "Thermodynamics of rare earth sesquioxides," *Prog. Mater. Sci.*, **52**(4), 597 (2007).
5. S. V. Ushakov and A. Navrotsky, "Experimental approaches to the thermodynamics of ceramics above 1500°C," *J. Am. Ceram. Soc.*, **95**(5), 1463 (2012).
6. H. L. Lukas, S. G. Fries, and B. Sundman, *Computational Thermodynamics*, New York: Cambridge University Press, 2007.
7. O. Kubaschewski, C. B. Alcock, and P. J. Spencer, *Materials Thermochemistry*, 6th ed. Oxford: Pergamon Press Ltd, 1993.
8. E. E. Shpil'rain, D. N. Kagan, and L. S. Barkhatov, "Thermodynamic properties of the condensed phase of alumina near the melting point," *High Temp.-High Press.*, **4**(6), 605 (1972).
9. S. V. Ushakov and A. Navrotsky, "Direct measurements of fusion and phase transition enthalpies in lanthanum oxide," *J. Mater. Res.*, **26**(7), 845 (2011).
10. S. Ansell, S. Krishnan, J. K. R. Weber, J. Felten, P. Nordine, M. Beno, D. Price, and M.-L. Saboungi, "Structure of liquid aluminum oxide," *Phys. Rev. Lett.*, **78**(3), 464 (1997).
11. L. B. Skinner, A. C. Barnes, P. S. Salmon, L. Hennet, H. E. Fischer, C. J. Benmore, S. Kohara, J. K. R. Weber, A. Bytchkov, M. C. Wilding, J. B. Parise, T. O. Farmer, I. Pozdnyakova, S. K. Tumber, and K. Ohara, "Joint diffraction and modeling approach to the structure of liquid alumina," *Phys. Rev. B*, **87**(2), 24201 (2013).
12. H. Itoh, S. Akira, M. Takashi, and Y. Toshio, "Electromotive-force measurements of molten oxide mixtures," *J. Chem. Soc.*, **80**, 473 (1984).
13. R. O. Colson, "In situ voltammetric observation of transitions above the liquidus in silicate melts," *Contrib. Mineral. Petr.*, **159**(5), 703 (2009).
14. R. O. Colson, A. M. Floden, T. R. Haugen, K. M. Malum, M. Sawarynski, M. K. B. Nermoe, K. E. Jacobs, and D. Holder, "Activities of NiO, FeO, and O_2- in silicate melts," *Geochim. Cosmochim. Acta*, **69**(12), 3061 (2005).
15. K. Takahashi and Y. Miura, "Electrochemical behavior of glass melts," *J. Non. Cryst. Solids*, **96**, 119 (1987).
16. Y. Miura, Y. Akiyama, and K. Takahashi, "Electrolysis of molten sodium borate glasses," *J. Ceram. Soc. Jpn.*, **94**(4), 425 (1986).
17. K. Kawamura and T. Yokokawa, "Linear sweep voltammetry of Pb2+/Pb in oxide melts," *J. Electrochem. Soc.*, **135**(6), 1447 (1988).
18. A. Sasahira, K. Kawamura, M. Shimizu, N. Takada, M. Hongo, and T. Yokokawa, "Pb2+/Pb redox equilibria in sodium borate, silicate, and aluminosilicate melts," *J. Electrochem. Soc.*, **136**(7), 1861 (1989).
19. P. F. Paradis, T. Ishikawa, G. W. Lee, D. Holland-Moritz, J. Brillo, W. K. Rhim, and J. T. Okada, "Materials properties measurements and particle beam interactions studies using electrostatic levitation," *Mater. Sci. Eng. R*, **76**(1), 1 (2014).
20. J. K. R. Weber, A. Tamalonis, C. J. Benmore, O. L. G. Alderman, S. Sendelbach, A. Hebden, and M. A. Williamson, "Aerodynamic levitator for in situ X-ray structure measurements on high temperature and molten nuclear fuel materials," *Rev. Sci. Instrum.*, **87**(7), 73902 (2016).
21. J. E. Enderby, S. Ansell, S. Krishnan, and D. L. Price, "The electrical conductivity of levitated liquids," *Appl. Phys. Lett.*, **71**(1), 116 (1997).
22. Y. Arai, P.-F. Paradis, T. Aoyama, T. Ishikawa, and S. Yoda, "An aerodynamic levitation system for drop tube and quenching experiments," *Rev. Sci. Instrum.*, **74**(2), 1057 (2003).
23. E. G. Lierke, "Acoustic levitation - a comprehensive survey of principles and applications," *Acustica*, **82**(2), 220 (1996).
24. D. Langstaff, M. Gunn, G. N. Greaves, A. Marsing, and F. Kargl, "Aerodynamic levitator furnace for measuring thermophysical properties of refractory liquids," *Rev. Sci. Instrum.*, **84**(12), 124901 (2013).
25. L. B. Skinner, C. J. Benmore, J. K. R. Weber, M. A. Williamson, A. Tamalonis, A. Hebden, T. Wiencek, O. L. G. Alderman, M. Guthrie, L. Leibowitz, and J. B. Parise, "Molten uranium dioxide structure and dynamics," *Science*, **346**(6212), 984 (2014).
26. L. B. Skinner, C. J. Benmore, J. K. R. Weber, J. Du, J. Neuefeind, S. K. Tumber, and J. B. Parise, "Low cation coordination in oxide melts," *Phys. Rev. Lett.*, **112**, 157801 (2014).
27. P. F. Paradis and T. Ishikawa, "Surface tension and viscosity measurements of liquid and undercooled alumina by containerless techniques," *Jpn. J. Appl. Phys. 1*, **44**(7A), 5082 (2005).
28. P. F. Paradis, T. Ishikawa, Y. Saita, and S. Yoda, "Non-contact thermophysical property measurements of liquid and undercooled alumina," *Jpn. J. Appl. Phys. 1*, **43**(4A), 1496 (2004).
29. M. R. Null and W. W. Lozier, "Carbon arc image furnaces," *Rev. Sci. Instrum.*, **29**(2), 163 (1958).
30. R. E. De La Rue and F. A. Halden, "Arc-image furnace for growth of single crystals," *Rev. Sci. Instrum.*, **31**(1), 35 (1960).
31. R. P. Poplawsky and J. E. Thomas, "Floating zone crystals using an arc image furnace," *Rev. Sci. Instrum.*, **31**(12), 1303 (1960).
32. W. G. Field and R. W. Wagner, "Thermal imaging for single crystal growth and its application to ruby," *J. Cryst. Growth*, **4**, 799 (1968).
33. K. Kitazawa, K. Nagashima, T. Mizutani, K. Fueki, and T. Mukaibo, "A new thermal imaging system utilizing a Xe arc lamp and ellipsoidal mirror for crystallization of refractory oxides," *J. Cryst. Growth*, **39**, 211 (1977).
34. J. J. Diamond and A. L. Dragoo, "Studies of molten alumina in the arc-image Furnace," *Rev. Hautes Temp. Refract.*, **3**(3), 273 (1966).
35. K. Eickhoff and K. Gürs, "Tiegelfreies zonenschmelzen von rubinkristallen durch aufheizen der schmelzzone mittels laser," *J. Cryst. Growth*, **6**, 21 (1969).
36. D. B. Gasson and B. Cockayne, "Oxide crystal growth using gas lasers," *J. Mater. Sci.*, **5**(2), 100 (1970).
37. L. S. Nelson, N. L. Richardson, K. Keil, and S. R. Skaggs, "Effects of oxygen and argon atmospheres on pendant drops of aluminum-oxide melted with carbon-dioxide laser radiation," *High Temp. Sci.*, **5**(2), 138 (1973).

38. S. Krishnan, J. K. R. Weber, R. A. Schiffman, P. C. Nordine, and R. A. Reed, "Refractive index of liquid aluminum oxide at 0.6328 μm," *J. Am. Ceram. Soc.*, **74**(4), 881 (1991).
39. T. Katsumata, T. Shiina, M. Shibasaki, and T. Matsuo, "Electrical measurements on molten TiO_2 using a floating zone furnace," *J. Cryst. Growth*, **239**, 1791 (2002).
40. "Standard test methods for apparent porosity, liquid absorption, apparent specific gravity, and bulk density of refractory shapes by vacuum pressure," *ASTM Standard C830-00 (2011)*, ASTM International, West Conshohocken, PA, 2011.
41. S. W. Hughes, "Archimedes revisited: a faster, better, cheaper method of accurately measuring the volume of small objects," *Phys. Educ.*, **40**(5), 468 (2005).
42. S. Sokhanvaran, S.-K. Lee, G. Lambotte, and A. Allanore, "Electrochemistry of molten sulfides: copper extraction from BaS-Cu2S," *J. Electrochem. Soc.*, **163**(3), D115 (2016).
43. A. M. Bond, D. Elton, S. X. Guo, G. F. Kennedy, E. Mashkina, A. N. Simonov, and J. Zhang, "An integrated instrumental and theoretical approach to quantitative electrode kinetic studies based on large amplitude Fourier transformed a.c. voltammetry: A mini review," *Electrochem. Commun.*, **57**, 78 (2015).
44. D. J. Gavaghan and A. M. Bond, "A complete numerical simulation of the techniques of alternating current linear sweep and cyclic voltammetry: analysis of a reversible process by conventional and fast Fourier transform methods," *J. Electroanal. Chem.*, **480**(1–2), 133 (2000).
45. S. O. Engblom, J. C. Myland, and K. B. Oldham, "Must ac voltammetry employ small signals?," *J. Electroanal. Chem.*, **480**(1–2), 120 (2000).
46. A. Allanore, L. Yin, and D. R. Sadoway, "A new anode material for oxygen evolution in molten oxide electrolysis.," *Nature*, **497**(7449), 353 (2013).
47. H. Kim, J. Paramore, A. Allanore, and D. R. Sadoway, "Electrolysis of molten iron oxide with an iridium anode: the role of electrolyte basicity," *J. Electrochem. Soc.*, **158**(10), E101 (2011).
48. M. S. Chandrasekharaiah, M. D. Karkhanavala, and S. N. Tripathi, "The pressure of iridium oxides over iridium at high temperatures in 1 atm of dry oxygen," *J. Less-Common Met.*, **80**(1), (1981).
49. D. Wang, A. J. Gmitter, and D. R. Sadoway, "Production of Oxygen Gas and Liquid Metal by Electrochemical Decomposition of Molten Iron Oxide," *J. Electrochem. Soc.*, **158**(6), E51 (2011).
50. C. H. P. Lupis, *Chemical Thermodynamics of Materials*, New York: North-Holland, 1983.
51. C. W. Bale, E. Bélisle, P. Chartrand, S. A. Decterov, G. Eriksson, A. E. Gheribi, K. Hack, I. H. Jung, Y. B. Kang, J. Melançon, A. D. Pelton, S. Petersen, C. Robelin., J. Sangster, and M.-A. Van Ende, "FactSage thermochemical software and databases, 2015–2016," *Calphad*, **54**, 35 (2016).
52. A. M. Brown and M. F. Ashby, "Correlations for diffusion constants," *Acta Metall.*, **28**(8), 1085 (1980).
53. D. R. Stull and H. Prophet, "JANAF thermochemical tables," U.S. Department of Commerce, Washington, 1985.
54. M. W. Chase, J. L. Curnutt, A. T. Hu, H. Prophet, A. N. Syverud, and L. C. Walker, "JANAF thermochemical tables, 1974 supplement," *J. Phys. Chem. Ref. Data*, **3**(2), 311 (1974).
55. M. E. Orazem and B. Tribollet, *Electrochemical Impedance Spectroscopy*, Hoboken: John Wiley & Sons, Inc., 2008.
56. A. E. van Arkel, E. A. Flood, and N. F. H. Bright, "The electrical conductivity of molten oxides," *Can. J. Chem.*, **31**(11), 1009 (1953).
57. H. Fay, "The electrical conductivity of liquid Al2O3 (molten corundum and ruby)," *J. Phys. Chem.*, **70**(3), 890 (1966).
58. V. P. Elyutin, B. S. Mitin, and Y. A. Nagibin, "Electrical conductivity of molten aluminum oxide," *Izv. Akad. Nauk SSSR, Neorg. Mater.*, **7**(5), 880 (1971).
59. V. I. Aleksandrov, V. V. Osiko, and V. M. Tatarintsev, "Electrical conductivity of aluminum oxide in the molten state," *Izv. Akad. Nauk SSSR, Neorg. Mater.*, **8**(5), 956 (1972).
60. E. E. Shpil'rain, D. N. Kagan, L. S. Barkhatov, and L. I. Zhmakin, "Experimental study of specific electrical conductivity of molten aluminum oxide at temperature up to 3000 K," *Teplofiz. Vys. Temp.*, **14**(5), 948 (1976).
61. B. Glorieux, M.-L. Saboungi, F. Millot, J. Enderby, and J.-C. Rifflet, "Aerodynamic levitation: an approach to microgravity," *AIP Conf. Proc.*, **552**, 316 (2001).
62. M. L. Saboungi, J. Enderby, B. Glorieux, H. Schnyders, Z. Sungaila, S. Krishnan, and D. L. Price, "What is new on the levitation front?," *J. Non. Cryst. Solids*, **312–314**, 294 (2002).
63. A. N. Shatunov, A. I. Maksimov, A. Y. Pechenkov, and I. V. Poznyak, "Method of electrical resistivity measurement for high-temperature melts," *Inorg. Mater.*, **47**(14), 1579 (2011).
64. S. J. Schneider, "Cooperative determination of the melting point of alumina," *Pure Appl. Chem.*, **21**, 115 (1970).
65. R. E. Bedford, G. Bonnier, H. Maas, and F. Pavese, "Recommended values of temperature on the International Temperature Scale of 1990 for a selected set of secondary reference points," *Metrologia*, **33**, 133 (1996).
66. F. Henning and H. T. Wensel, "The freezing point of iridium," *Bur. Stand. J. Res.*, **10**(6), 809 (1933).
67. E. Thibodeau and I. H. Jung, "A structural electrical conductivity model for oxide melts," *Metall. Mater. Trans. B*, **47**(1), 355 (2016).